

Chapter 6

Systematic Uncertainties

6.1 Introduction

There were two classes of systematic uncertainties for $P_\mu^\pi \xi$: those related to the accuracy of the P_μ simulation, and a separate group from the decay positron reconstruction. The latter were evaluated simultaneously for ρ , δ and $P_\mu^\pi \xi$, by exaggerating an effect in the simulation or the analysis software; the exaggerated spectrum was then fit against the original spectrum to determine the change in the muon decay parameters (MPs). The exaggeration factors were made as large as possible to obtain a statistically meaningful MP change (“sensitivity”), while maintaining a linear relationship with the MPs. The changes in MPs were scaled down according to how large the effect could actually be, resulting in the systematic uncertainty. When the original and exaggerated spectra were highly correlated (*i.e.* they contained a large number of events with identical energy and angle), the uncertainties in the MP differences were scaled down until the reduced χ^2 from the fitting procedure was equal to one.

6.2 Overview

The $P_\mu^\pi \xi$ uncertainties for the nominal sets are summarised in Table 6.1, from which it is clear that the measurement is limited by the accuracy of the muon beam and the solenoidal fringe field. The entries in this table will be described fully in the current chapter. The table indicates three statistical uncertainties; these could have been reduced by accumulating more data and/or simulation under the same running conditions. The most recent TWIST analysis (MacDonald '08 in the table) did not re-evaluate the polarisation uncertainties, since it was a measurement of ρ and δ . A selection of the systematic uncertainties were set dependent, and in these cases Table 6.1 contains the uncertainty for the nominal sets only. Note that the set dependent corrections will be presented at the end of the chapter.

Table 6.1: Summary of $P_\mu^\pi \xi$ uncertainties. The statistical uncertainties are marked (stat.); otherwise the uncertainties are systematic. For this analysis, (0) indicates the uncertainty is no longer evaluated.

Category	Thesis section	New eval.?	Uncertainty ($\times 10^{-4}$)		
			This analysis	MacDonald '08 [10, 18]	Jamieson '06 [21, 57]
Extraction of $\Delta P_\mu^\pi \xi$ (stat.)	7.1	✓	2.4*	3.7	6
Polarisation					
Production target	6.3.1	✓	0.4	2.1	2.1
μ^+ beam/ fringe field	6.3.2	✓	11.3,14.9^a	34.0	34.0
Stopping material					
λ (stat.)	6.3.3	✓	3.0	Not eval.	Not eval.
$P_\mu(t)$ model	6.3.3	✗	(0)	12	12
Background muons	6.3.4	✓	1.0	2	1.8
Beam intensity	6.3.5	✓	*	0.2	1.8
Chamber response					
DC STR	6.4.1	✓	0.0	6.0	Not eval.
Wire time offsets	6.4.2	✓	*	0.4	8.9
US-DS efficiency	6.4.3	✓	*	1.1	1.9
Dead zone	6.4.4	✓	*	0	0.1
Foil bulge	6.4.5	✗	(0)	0.7	2.2
Cell asymmetry	6.4.6	✗	(0)	0	2.2
Density variations	6.4.7	✗	(0)	0.2	0.2
Alignment					
z length scale	6.5.1	✗	0.7	0.7	2.2
u/v width scale	6.5.2	✗	0.2	0.2	Not eval.
DC alignment	6.5.3	✗	0.02	0.02	2.2
B-field to axis	6.5.4		*	Not eval.	0.3
Positron interactions					
δ -electron rate	6.6.1	✓	*	1.4	2.9
Bremsstrahlung rate	6.6.2	✓	*	0.03	
Outside material	6.6.3	✓	*	0.6	0.2
Multiple scattering	6.6.4	✗	(0)	0	0.8
Energy loss	6.6.5	✗	0.01	0.01	0.1
Resolution	6.7	✗	0.7	0.7	Not eval.
Momentum calibration					
Tracking B-field	6.8.1	✓	*	1.1	0.9
Kinematic endpoint					
Parameters (stat.)	6.8.2	✓	*	0.5	1.6
Propagation	6.8.2	✓	*	0.09	
External					
Radiative corrections	6.9.1	✗	0.5	0.5	1.0
η correlation	6.9.2	✗	1.1	1.1	Not eval.

^a For the nominal sets in 2006 (silver target), the uncertainty is 11.3×10^{-4} . In 2007 (aluminium target), the uncertainty is 14.9×10^{-4} . The larger uncertainty in 2007 is due to the lower quality of the muon beam tune.

6.3 Polarisation

6.3.1 Production target

The simulation generated muons with anti-parallel spin and momentum vectors, starting from the end of the M13 beam line. This neglected multiple scattering in the graphite production target and the beam line vacuum window, which changed the momentum vector but not the spin. This is treated here as a systematic correction with an associated uncertainty. (The difference in precession frequencies of the momentum and spin through the M13 beam line is neglected since it introduced an error of $< 10^{-8}$; see Appendix I).

Surface muons are produced with $p \approx 29.79 \text{ MeV}/c$, but the beam line was nominally tuned to accept muons with an average momentum of $\langle p \rangle = 29.6 \text{ MeV}/c$. Therefore the muons lost $0.19 \text{ MeV}/c$ of momentum on average, which is equivalent to $\approx 3.8 \text{ mg}/\text{cm}^2$ in graphite. The width of the resulting multiple scattering distribution, θ_0 , was estimated using a **GEANT4** simulation. As a consistency check, the same estimate was made using an approximate expression from the Particle Data Group (PDG)[3], and two further approximations from Ref. [99] that are intended to be more accurate than the PDG. The results for θ_0 varied from 8.2 mr to 12.0 mr , and are shown in Table 6.2. The degree to which the spin is depolarised with respect to momentum is then estimated by $\cos(\theta_{\text{space}}^{\text{rms}})$, where $\theta_{\text{space}}^{\text{rms}} = \sqrt{2} \theta_0$. The central value of the correction was taken as the **GEANT4** result, since it was believed to be the most accurate of the estimates. The uncertainty in the correction was half of the range of the four θ_0 estimates.

The evaluations were repeated for the lower momentum sets at $\langle p \rangle = 28.75 \text{ MeV}/c$ and $\langle p \rangle = 28.85 \text{ MeV}/c$, and these results are included in Table 6.2. Later the consistency of $\Delta P_{\mu}^{\pi} \xi$ between the nominal and lower momentum sets (after correction) will be demonstrated.

These estimates did not include the $3 \mu\text{m}$ beam line vacuum window that the muons passed through. This was safely neglected since it corresponded to just $0.3 \text{ mg}/\text{cm}^2$ of material, which is an order of magnitude less than the average material traversed in the production target.

The previous $P_{\mu}^{\pi} \xi$ analysis found a systematic uncertainty of 2×10^{-4} due to depolarisation in the production target; this was evaluated as a conservative upper limit, rather than making a correction[57].

Table 6.2: $\Delta P_\mu^\pi \xi$ correction due to multiple scattering within the graphite production target. The uncertainty is estimated from the spread of θ_0 values from the four estimates.

Beam tune	Lower momentum		Nominal
Beam line $\langle p \rangle$ (MeV/c)	28.75	28.85	29.60
Momentum loss in graphite (MeV/c)	1.04	0.94	0.19
Graphite thickness ^a			
(mg/cm ²)	18.9	17.2	3.8
($\times 10^{-4} X_0$) ^b	4.43	4.03	0.89
Scattering distribution width, θ_0 (mr) ^c			
GEANT4	24.2	22.9	9.3
Simple PDG estimate[3]	25.3	24.0	10.4
Eq. (6) of Ref. [99]	28.9	27.4	12.0
Eq. (7) of Ref. [99]	22.8	21.5	8.2
$P_\mu^\pi \xi$ correction ($\times 10^{-4}$)	-5.9 ± 1.6	-5.2 ± 1.4	-0.9 ± 0.4

^a The range estimate assumed only ionisation energy losses, and used the Bethe-Bloch formula in the continuous slowing down approximation.

^b X_0 = one radiation length (42.7 g/cm² for graphite).

^c θ_0 is the standard deviation of a Gaussian fit to the central 98% of the the plane-projected multiple scattering distribution.

6.3.2 Muon beam and fringe field

Overview

The simulation transported the muon spin from the end of the M13 beam line to the metal stopping target. This relied on the accuracies of the muon beam measurement and the magnetic field map, both of which will contribute to the assessment of the $P_\mu^\pi \xi$ uncertainty.

The systematic uncertainties from the muon beam and fringe field are summarised in Table 6.3. These will now be described in detail. First a correction will be made to the $P_\mu^\pi \xi$ result based on an improved magnetic field map, and remaining uncertainties in the map will be considered. Then the uncertainties in the muon beam will be included. These will be separated into two approximately orthogonal parts: contributions from the average position/angle of the beam, and those from the width of the beam’s angular distributions.

The term “fringe field” will refer to the magnetic field from the end of the M13 beam line up to the first drift chamber ($-200 \text{ cm} < z < -50 \text{ cm}$). It is assumed that the reader is familiar with the solenoidal magnet (Section 2.7), the measurement of the magnetic field map (Appendix D), the parameters of the muon beam inside the detector (Section 3.7), and the available data sets (Section 5.3).

Table 6.3: Summary of muon beam and fringe field uncertainties, for sets with a nominal beam tune. The muon beam uncertainties were different for the data in 2006 (silver target) and 2007 (aluminium target).

Description	Uncertainty ($\times 10^{-4}$)
Fringe field 1 mT variations	4
μ^+ beam: A not matched	5
μ^+ beam: TEC and field alignment	7 (2006), 12 (2007) ^a
Simulation of multiple scattering	5
Noise from TEC electronics	2.2
Aging of TEC sense planes	2.6
Quadratic sum	11.3 (2006), 14.9 (2007)

^a The beam in 2007 was lower quality.

Measures of difference in polarisation

In the following discussion, $P_\mu(0)$ is the average z -component of the muon's spin in the simulation, at the metal target, *before* any time dependent depolarisation has taken place. This is not an absolute polarisation, and is only used to evaluate the relative sensitivity of $\Delta P_\mu^\pi \xi$ to uncertainties in the magnetic field and muon beam measurement. Since the simulation knows the spin of each muon exactly, $P_\mu(0)$ can be determined with high precision using a relatively small number of muons. The $P_\mu(0)$ values in this section used simulations with 0.1×10^6 muons, which resulted in a statistical uncertainty of 0.1×10^{-4} for nominal sets, and 0.2×10^{-4} for sets with a steered beam profile.

For the data, the difference between two decay positron spectra can measure $\Delta P_\mu^D \xi$, where P_μ^D is the average polarisation at the time of decay. The quantity $\Delta P_\mu^D \xi$ was validated to be directly comparable to the difference between two $P_\mu(0)$ values from the simulation.

Two of the data sets used muon beams that were steered away from the solenoid's symmetry axis. As a result of this steering, the beams experienced larger transverse fringe field components, and the muons underwent more depolarisation than for the nominal sets. The degree to which the simulation can reproduce the difference in polarisation between a nominal and steered beam will contribute to the discussion of the systematic uncertainty. From the data, a spectrum fit between the nominal and steered sets found

$$\Delta P_\mu^{74-76}(0) = (101 \pm 8) \times 10^{-4}, \quad (6.1)$$

$$\Delta P_\mu^{87-86}(0) = (59 \pm 7) \times 10^{-4}, \quad (6.2)$$

where the superscripts (74-76) and (87-86) refer to the set numbers in Table 5.1. From here on, these quantities will be referred to as ΔP_μ^{74-76} and ΔP_μ^{87-86} .

Fringe field correction: motivation

The on-axis longitudinal component of the fringe field is shown in Fig. 6.1(a). This steadily increased in magnitude from the yoke door entrance to the drift chamber (DC) tracking region. The on-axis transverse field components were negligible; instead the *off-axis* values are shown in Fig. 6.1. These components were radially symmetric, and they were strongly correlated with the muon's depolarisation, which is shown for a nominal and steered beam in Fig. 6.2(a). The transverse field components were maximised just inside the door, at which point the muons started to undergo depolarisation that continued until the first DC at $z = -50$ cm. The quality of the fringe field downstream of the door was important since it controlled the rate of depolarisation. The field upstream of the door was also important

since it affected which part of the fringe field the beam was transported through. The average x -positions of the same beams are shown in Fig. 6.2(b). The steered beam passes through a part of the fringe field with larger transverse field components, resulting in a significantly greater depolarisation.

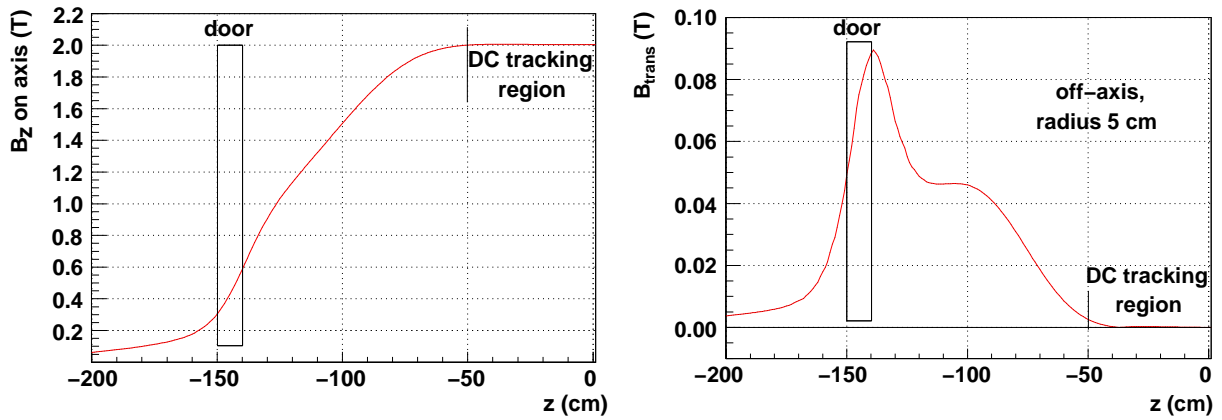
The analysis used a fringe field map that was generated with the OPERA software package[83], which had accuracy limitations. Most importantly, the software used a finite element method to solve Maxwell's equations, and the 40 cm diameter circular hole in the yoke door was expected to introduce difficulties in this modelling³⁶. (The hole was in a critical region for the transverse field components, and hence the depolarisation.) Also, the field map used for the analysis did not include the steel in the floor of the M13 area and the final M13 quadrupoles.

The B_z components from OPERA are compared to measurements from Hall probes in Fig. 6.3(a). Only the z components are shown since the Hall probes were single axis, and did not measure B_x and B_y . Extensive efforts were made to resolve the observed disagreement by adjusting the OPERA inputs, such as the solenoid's coil positions in $x/y/z$, the radii of these coils and their current densities, the $B - H$ curve for the iron yoke, and the position of the door in z . The previous $P_\mu^\pi \xi$ measurement found that variations in these inputs affected $P_\mu(0)$ by 3×10^{-4} at most[57]; as a result of this low sensitivity, and the limitations of the finite element analysis, the tuning of OPERA was not pursued further.

For this measurement an attempt was made to overcome the limitations of the finite element method. An additional field from three on-axis coils was added to the OPERA map; the coils were located at $z = -200$ cm*, -150 cm, -140 cm, with radii *, *, * and their central field strengths were *, * and *. This approach was motivated by observing that Fig. 6.3(a) resembled the field from a pair of gradient coils. We feel it is not a coincidence that the coils' z -locations corresponded to the outer and inner sides of the yoke door where the circular hole was located, and the last M13 quadrupole, which was not included in OPERA. Resolving this discrepancy will be seen to change $P_\mu(0)$ by significantly more than the uncertainties from the previous measurement.

The apparatus that supported the Hall probes had alignment limitations: the Hall probes were attached to an arm that was deflected by gravity, introducing a vertical misalignment of up to 0.1 cm, and the whole mapping device was aligned in the yoke's coordinate system to about 0.2 cm in x and y . A comparison of the Hall probes and OPERA could not produce a precise translational alignment in x and y , but the position of the muon beam inside the

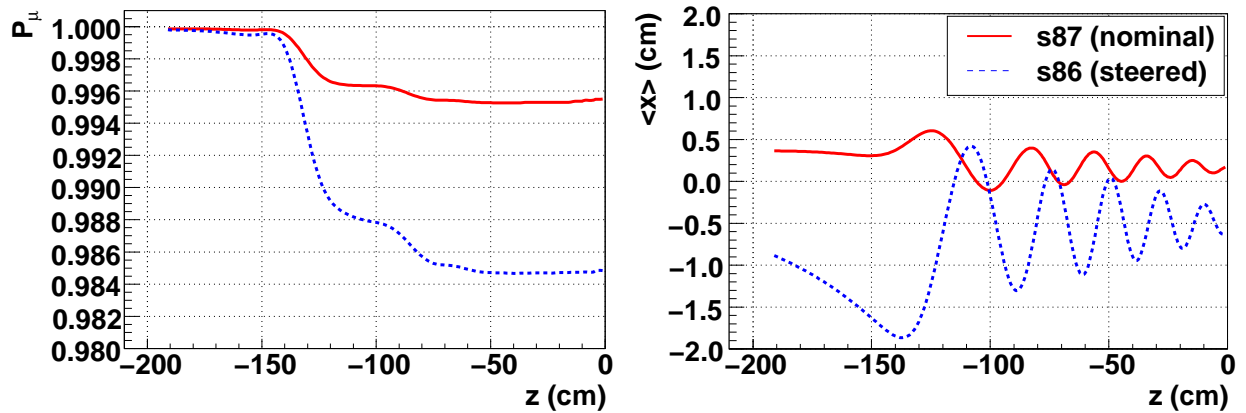
³⁶Specifically, finite element analyses are expected to encounter difficulties when there are scales involved that are several orders of magnitude apart. In this case, the important region for the depolarisation of the muons is within $\lesssim 4$ cm of the axis (see Fig. 6.2(b)), there is a circular hole in the yoke of diameter 40 cm, and the whole map must be determined over a z -length of about 5 m.



(a) B_z component, on-axis ($x = y = 0$).

(b) Transverse \vec{B} component at 5 cm radius. These components are radially symmetric.

Figure 6.1: Fringe field components from the OPERA finite element analysis.



(a) Simulation: average z component of the muon's spin (" P_μ ").

(b) Simulation: average x position of the muon beam.

Figure 6.2: Polarisation and mean position for a nominal and steered beam.

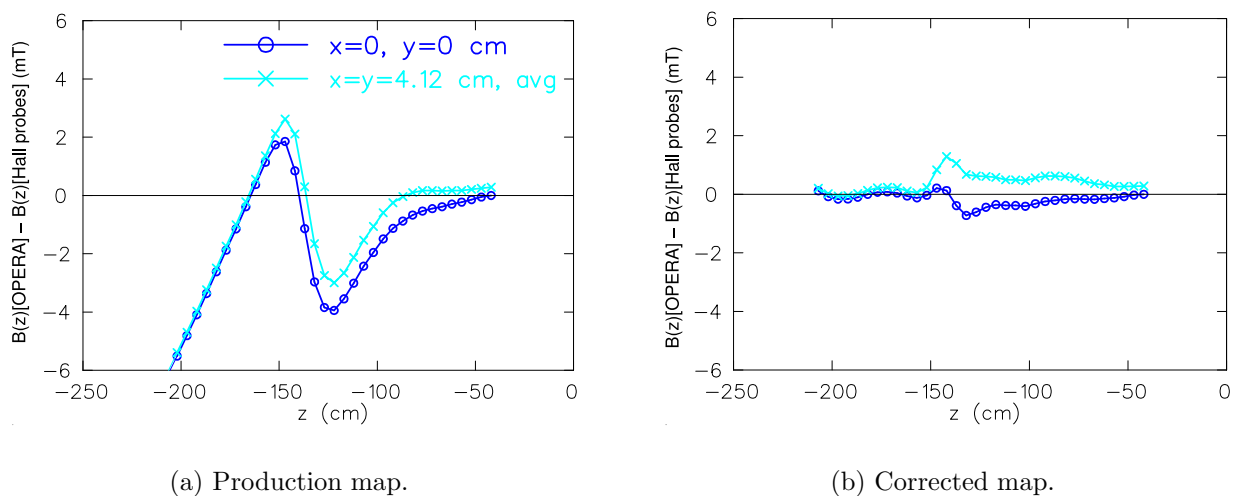


Figure 6.3: Difference in B_z between the magnetic field maps from OPERA and the Hall probes. Two comparisons are shown: the on-axis ($x = y = 0$) and an off-axis average of $x = \pm 4.12$ cm, $y = \pm 4.12$ cm. The corrected map has three current loops added. Muons start in the simulation at $z = -191.944$ cm.

detector did have sensitivity. On a set-by-set basis, a field translation was determined such that the data and simulation positions matched. On average, this required a translation of the entire map by $(\Delta x, \Delta y) = (0.18, 0.19)$ cm. Although this translation was determined precisely, we cannot be sure that it was accurate for a number of reasons. First, the position of the internal muon beam was also sensitive to the solenoid's coil positions³⁷. Second, the field through the hole in the yoke should be constrained to have its symmetry axis through the centre of the hole. Third, the translation was determined from beam profiles that will later be shown to suffer from their own alignment uncertainties. Also the translation may be compensating for the residual discrepancies in the field map (see Fig. 6.3(b)).

Fringe field correction: P_μ sensitivity

The set-by-set changes in $P_\mu(0)$ between the OPERA and corrected fringe field maps are shown in Table 6.4 and Fig. 6.4. The corrected map reduced the apparent polarisation in all cases. For the sets that used the silver target and a nominal beam profile, the $P_\mu(0)$ change between OPERA and the corrected map (with translation) was between -9×10^{-4} (set 71) and -17×10^{-4} (set 75). For the aluminium target and a nominal beam profile, the change

³⁷A change in the solenoid coil positions by ≈ 1 cm caused the internal muon beam to move by about ≈ 0.3 cm. The coil positions were known to ≈ 0.2 cm[100].

was between -20×10^{-4} (set 91) and -29×10^{-4} (set 83). The increased sensitivity for the aluminium target sets was due to the lower quality of the muon beam³⁸. As expected, the steered beam profiles were even more sensitive to the maps, with changes of -36×10^{-4} (set 76) and -100×10^{-4} (set 86). Note that from this point onwards, the corrected fringe field map is used to evaluate $\Delta P_\mu^\pi \xi$ uncertainties.

Fringe field correction: residual mismatch

The corrected map that was shown in Fig. 6.3(b) still contains discrepancies at the $\lesssim 1$ mT level. A systematic uncertainty due to uncertainties in the field map can be estimated by determining how much features at the 1 mT level affect $P_\mu(0)$.

Two new fringe field maps were produced, with the currents in all three coils scaled by $\pm 10\%$. A further two maps had only the two coils at the yoke hole scaled by $\pm 10\%$. The comparison between OPERA and the new maps are shown in Fig. 6.5. For each map a simulation found the range in $P_\mu(0)$ values: for sets 74 and 87 (both nominal), the range was $0.9961 \rightarrow 0.9968$ and $0.9950 \rightarrow 0.9958$ respectively, and for sets 76 and 86 (both steered), the range was $0.9838 \rightarrow 0.9857$ and $0.9826 \rightarrow 0.9862$. The systematic uncertainty is half of these ranges, corresponding to $\pm 4 \times 10^{-4}$ for the nominal sets, $\pm 11 \times 10^{-4}$ for set 76, and $\pm 18 \times 10^{-4}$ for set 86.

³⁸For the data accumulated with the aluminium target, a vertical aperture was in place within the M13 beam line. As a result the slits and jaws at the frontend of M13 were opened wider, and the beam was not as well focussed at F3. In addition, muons with $y > 1.0$ cm at the TECs did not converge towards the solenoid's axis.

Table 6.4: Relative polarisation for the simulation, for different field maps.

Set num.	Target	Description	OPERA map	Corrected field map $P_\mu(0)$	
			$P_\mu(0)^a$	No translation	Translated ^b
68	Ag	Stopping distrib. peaked $\frac{1}{3}$ into target	0.9978	0.9965	0.9968
70	Ag	B = 1.96 T	0.9975	0.9962	0.9962
71	Ag	B = 2.04 T	0.9969	0.9960	0.9959
72	Ag	TECs-in, nominal beam	0.9947	0.9901	0.9898
74	Ag	Nominal A	0.9975	0.9965	0.9963
75	Ag	Nominal B	0.9977	0.9960	0.9965
76	Ag	Steered beam A	0.9922	0.9847	0.9886
83	Al	Downstream beam package in place	0.9978	0.9949	0.9958
84	Al	Nominal C	0.9977	0.9954	0.9960
86	Al	Steered beam B	0.9931	0.9842	0.9831
87	Al	Nominal D	0.9978	0.9954	0.9964
91	Al	Lower momentum I	0.9969	0.9949	0.9955
92	Al	Lower momentum II	0.9966	0.9945	0.9952
93	Al	Lower momentum III	0.9967	0.9947	0.9951

^a This is not the absolute polarisation of the simulation. See Section 6.3.2.

^b The entire field map was moved by $(\Delta x, \Delta y) = (0.18, 0.19)$ cm.

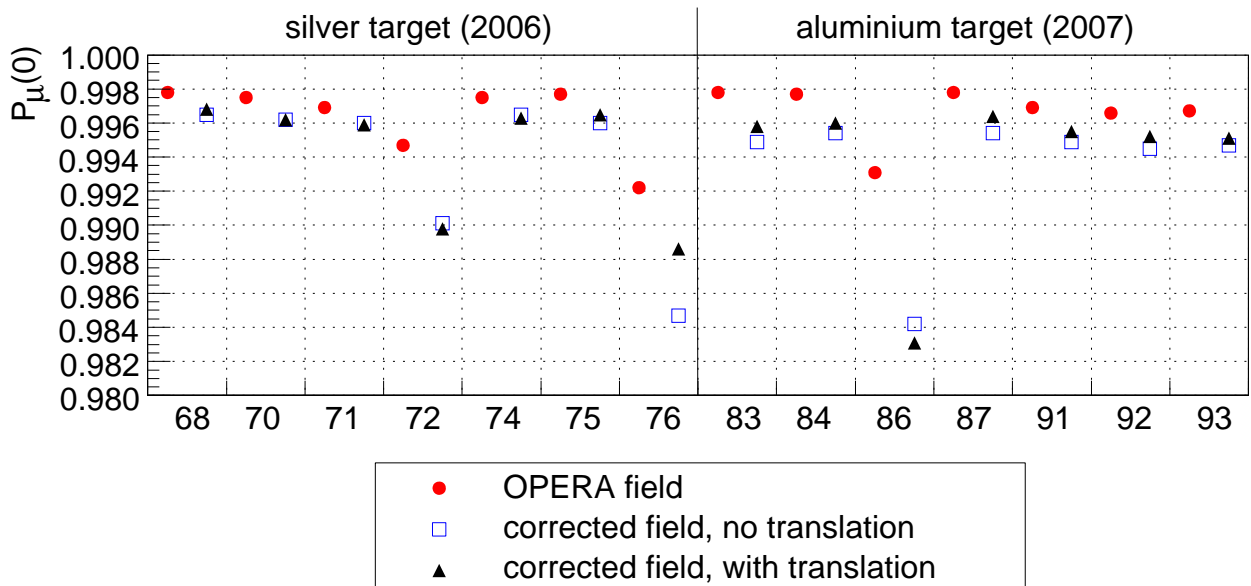


Figure 6.4: Relative polarisation for the simulation, for different field maps.

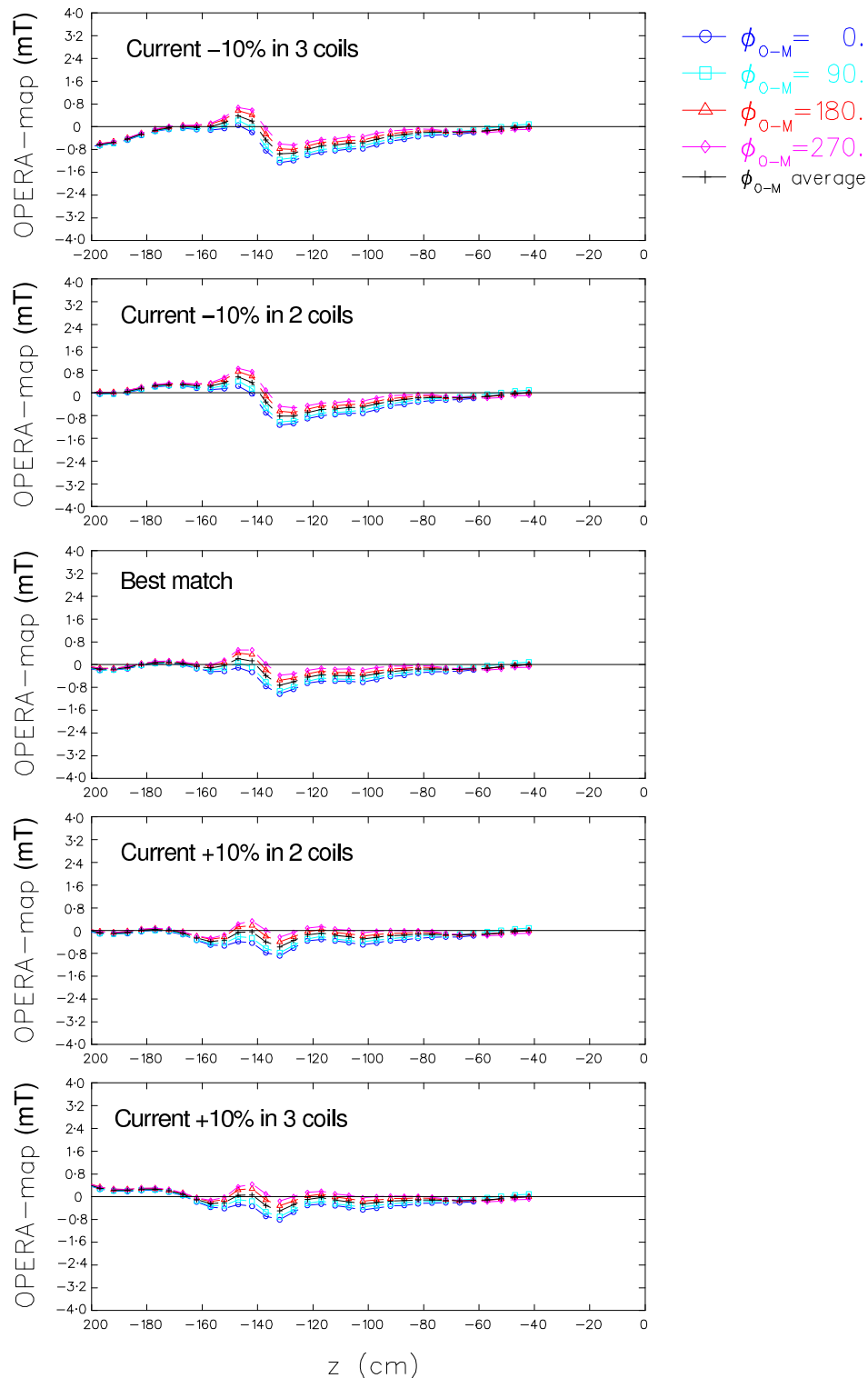


Figure 6.5: The difference between several corrected fringe field maps and the Hall probe measurements. These maps have residual features at the ≈ 1 mT level. The differences are taken on-axis ($x = y = 0$ cm), and each line shows the discrepancy for a different azimuthal angle. The variation with azimuthal angle indicates that the Hall probes were at an angle to symmetry axis of the field.

Muon beam: uncertainty in initial position and angle

A beam measurement was made with the TECs at the beginning and end of most data sets. The differences in the average positions and angles between these measurements are listed in Table 6.5, where changes of up to 0.18 cm in position and 3 mr in angle were observed. The origin may have been muon beam instability, a limitation in the reproducibility of the TECs, or an instability in the TEC drift cell response. Each of these will now be discussed.

Table 6.5: Muon beam differences for the beginning and end of set TEC measurements.

Set	Target	Description	$\Delta \langle x \rangle$ (cm)	$\Delta \langle y \rangle$ (cm)	$\Delta \langle \theta_x \rangle$ (mr)	$\Delta \langle \theta_y \rangle$ (mr)	ΔT^a (°C)
68	Ag	Stopping distrib. peaked $\frac{1}{3}$ into target	0.11	-0.05	0.2	-3.2	-0.3
70	Ag	B = 1.96 T	0.03	0.00	1.0	-0.4	-1.2
71	Ag	B = 2.04 T	0.09	-0.05	0.0	0.1	2.4
74	Ag	Nominal A ^b	-				
75	Ag	Nominal B	0.04	-0.10	-0.5	1.5	3.2
76	Ag	Steered beam	-0.04	-0.06	-0.6	1.9	1.3
83	Al	Downstream beam package in place	0.12	-0.09	0.6	0.7	-0.3
84	Al	Nominal C	0.18	-0.15	0.2	1.4	-0.4
86	Al	Steered beam B	0.04	-0.01	1.0	-0.01	-0.4
87	Al	Nominal D	0.13	-0.11	-0.1	0.7	-1.3
91/92/93	Al	Lower momentum ^b	-				

^a $\Delta T = T_{\text{end}} - T_{\text{start}}$. $\Delta T > 0$ indicates a temperature rise between measurements.

^b These sets only had one TEC measurement.

Muon beam instabilities were caused by a change in the proton beam upstream of the production target, or an instability in the M13 beam line elements. A special test displaced the proton beam at the production target by ± 0.1 cm vertically, which is about five times larger than the beam could have moved during normal operation³⁹. The largest observed TEC changes in the muon beam were $\Delta \langle y \rangle = \pm 0.07$ cm in position and $\Delta \langle \theta_y \rangle = \pm 1.0$ mr in angle, which are negligible after scaling down by a factor of five.

The settings of the M13 beam line elements (*e.g.* quadrupoles, dipoles, slits, jaws, asymmetric currents for quadrupole steering) were all monitored with a slow control system,

³⁹The proton beam was surrounded by four counters (top, bottom, left, right). In order to steer the beam vertically by 0.1 cm and avoid destroying the top or bottom counter, the proton beam current was reduced from the nominal setting of $\approx 100 \mu\text{A}$ to $\approx 20 \mu\text{A}$. This suggests that during normal operation, the proton beam could not have moved by more than $\approx 20/100 \times 0.1 \text{ cm} = 0.02 \text{ cm}$.

and runs with an instability were eliminated (see Section 5.4). Sets 72 had the TECs in place throughout, and found that the average muon beam position and angle were stable to < 0.02 cm and < 1 mr respectively (see Fig. 5.2). The muon beam measurement from the wire chambers was used to monitor stability for the nominal sets, which did not have the TECs in place. The sensitivity of the internal beam to M13 instabilities was determined by adjusting the currents in each quadrupole and dipole by $\pm 5\%$. An examination of the internal beam found that the largest variations were 0.02 cm in position, which corresponded to a conservative $P_\mu(0)$ change of 3×10^{-4} for the nominal beam tune. Instabilities in the muon beam do not explain the differences between beginning and end of set measurements in Table 6.5.

The space-time-relationship in the TEC drift cells depended on temperature. A change of $\pm 3^\circ\text{C}$ altered the average reconstructed positions by between 0.028 cm and 0.050 cm, depending on the average position of the beam within the module. (The x -positions increased with temperature and the y -positions decreased; see Ref. [76] for further detail.) The changes in angle were all < 0.05 mr, except for set 76, which still only changed by 0.4 mr. The temperature differences in Table 6.5 are not correlated with the change in average beam parameters, ruling out temperature as the dominant cause of the beginning/end of set differences.

The insertion/removal of the TECs required the beam line elements to be switched off, and a breaking of the vacuum in the beam line, which then had to be pumped down again before the TECs could be used. This process exerted significant forces on the beam line components and the box containing the TECs, and these forces are the prime candidate for the measured variation in average initial position and angle.

Muon beam: wire chamber measurements

An attempt was made to match the simulation’s “internal muon beam” (as measured by the wire chambers) to the data, using the degrees of freedom have been established (magnetic field translation, average position/angle of beam at the TECs). The resulting internal beam positions are shown in Fig. 6.6. For the nominal sets, the position in data and simulation match after applying the magnetic field translation and a combination of changes in TEC position and angle, of which there are a family of possible solutions. The positions from the steered beam profiles do not match the data for the allowed ranges. This supports the earlier observation that the corrected field map still has imperfections, and the steered beam profiles are more sensitive to them. There is no explicit systematic uncertainty from the position matching for *nominal* sets, since data and simulation can be brought into agreement with a translation of the fringe field that is within its alignment uncertainties.

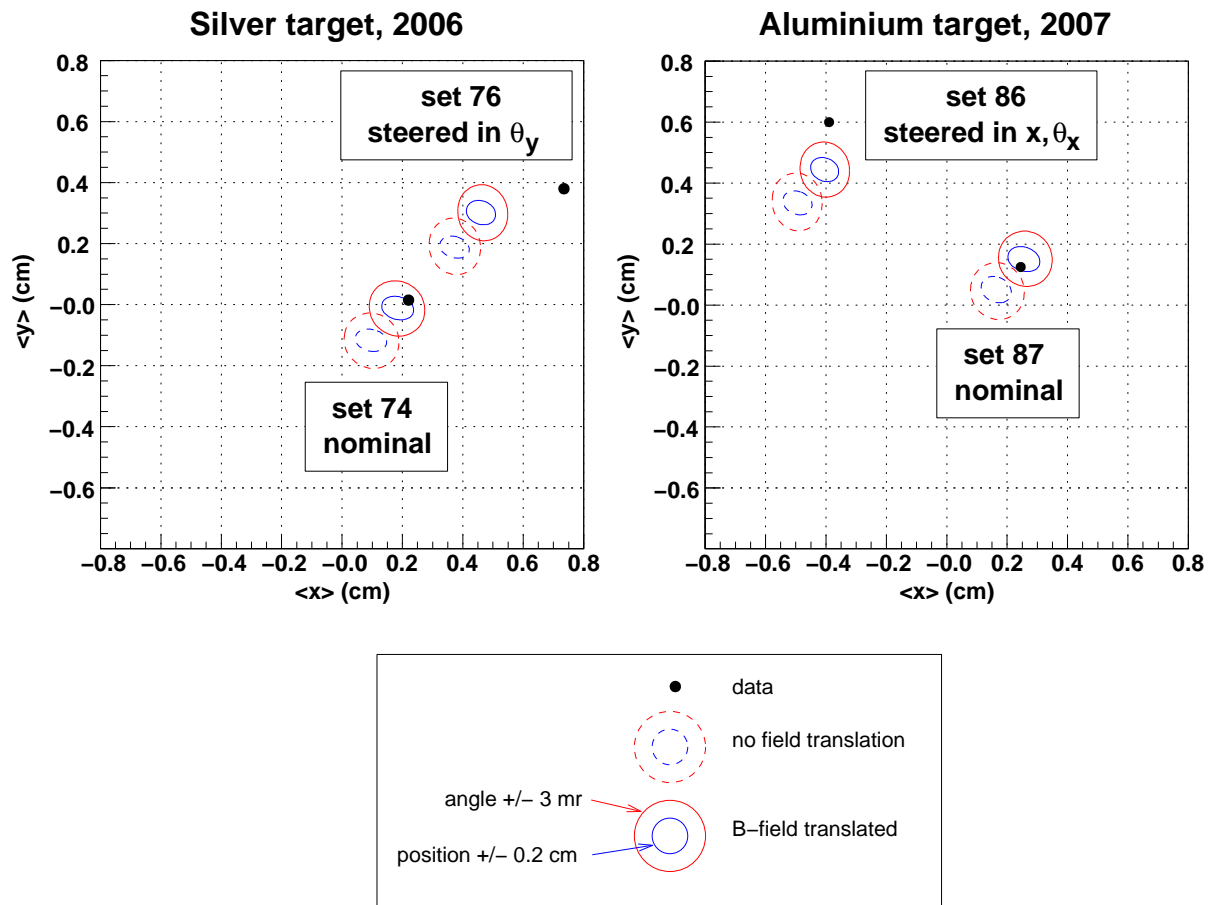


Figure 6.6: Internal muon beam position, as measured by the wire chambers. The spread in the simulation's position is due to uncertainties from the reproducibility of the TECs and the translation of the magnetic field.

The amplitude of muon beam oscillations in the detector, A , is a measure of the mean transverse momentum of the beam. (The root-mean-square beam size at each pair of planes also provides a measure, but this was found to have little sensitivity to the field map and initial beam position/angle). The data and simulation are compared Fig. 6.7, where there is no preference for translating the magnetic field. If the approximately quadratic dependence of $P_\mu(0)$ on A is extrapolated to match the data for sets 74 and 86, and interpolated for sets 76 and 87, then ΔP_μ^{74-76} and ΔP_μ^{87-86} from the simulation are

$$\Delta P_\mu^{74-76}(0) = (106 \pm 3) \times 10^{-4}, \quad (6.3)$$

$$\Delta P_\mu^{87-86}(0) = (73 \pm 2) \times 10^{-4}, \quad (6.4)$$

where the uncertainties here are from the spread in the data values, which are represented as a band in Fig. 6.7. Data and simulation now match for ΔP_μ^{74-76} (see Eq. (6.1)), but ΔP_μ^{87-86} disagrees by 14×10^{-4} ; however, this is within the $\pm 18 \times 10^{-4}$ that was observed from field map variations at the 1 mT level in an earlier section. Note that set 86 was carefully tuned to ensure the TECs did not clip the muon beam during measurement (otherwise this would have resulted in a different beam when the TECs were removed). Also, a simulation with the TECs in place confirmed that the same fraction of muons were missing the trigger scintillator for a nominal and the set 86 beam profile⁴⁰.

The ΔP_μ^{74-76} and ΔP_μ^{87-86} results suggest that $P_\mu(0)$ should be corrected so that A matches in data and simulation. For the nominal sets 74 and 87, this corresponds to correcting $P_\mu(0)$ from the ‘‘Translated’’ column of Table 6.4 by $+5 \times 10^{-4}$ and $+3 \times 10^{-4}$. However, this correction is determined using an imperfect fringe field map, and it should not be applied with confidence. Instead, the larger of the corrections ($\pm 5 \times 10^{-4}$) is taken as a contribution to the overall systematic uncertainty. There is also an uncertainty given by the range of $P_\mu(0)$ values from the magnetic field translation and TEC reproducibility. For the nominal sets 74 and 87, this is $\pm 7 \times 10^{-4}$ and $\pm 12 \times 10^{-4}$ respectively.

The phase and wavelength of the muon beam oscillations were also investigated. For the nominal beam, these were poorly determined and were not useful in making comparisons between data and simulation. The parameters for the steered beam sets were determined better, and are shown in Fig. 6.8. For set 76, a match in λ and ϕ is possible for a family of TEC displacements and rotations, but these parameters do not allow $P_\mu(0)$ to be constrained. For

⁴⁰Events were only analysed in the TECs if there was a signal at the trigger scintillator. There was a concern that the extra multiple scattering of the TECs would increase the beam size at the trigger scintillator, such that the muons would start to miss the trigger that would otherwise enter the spectrometer when the TECs were removed.

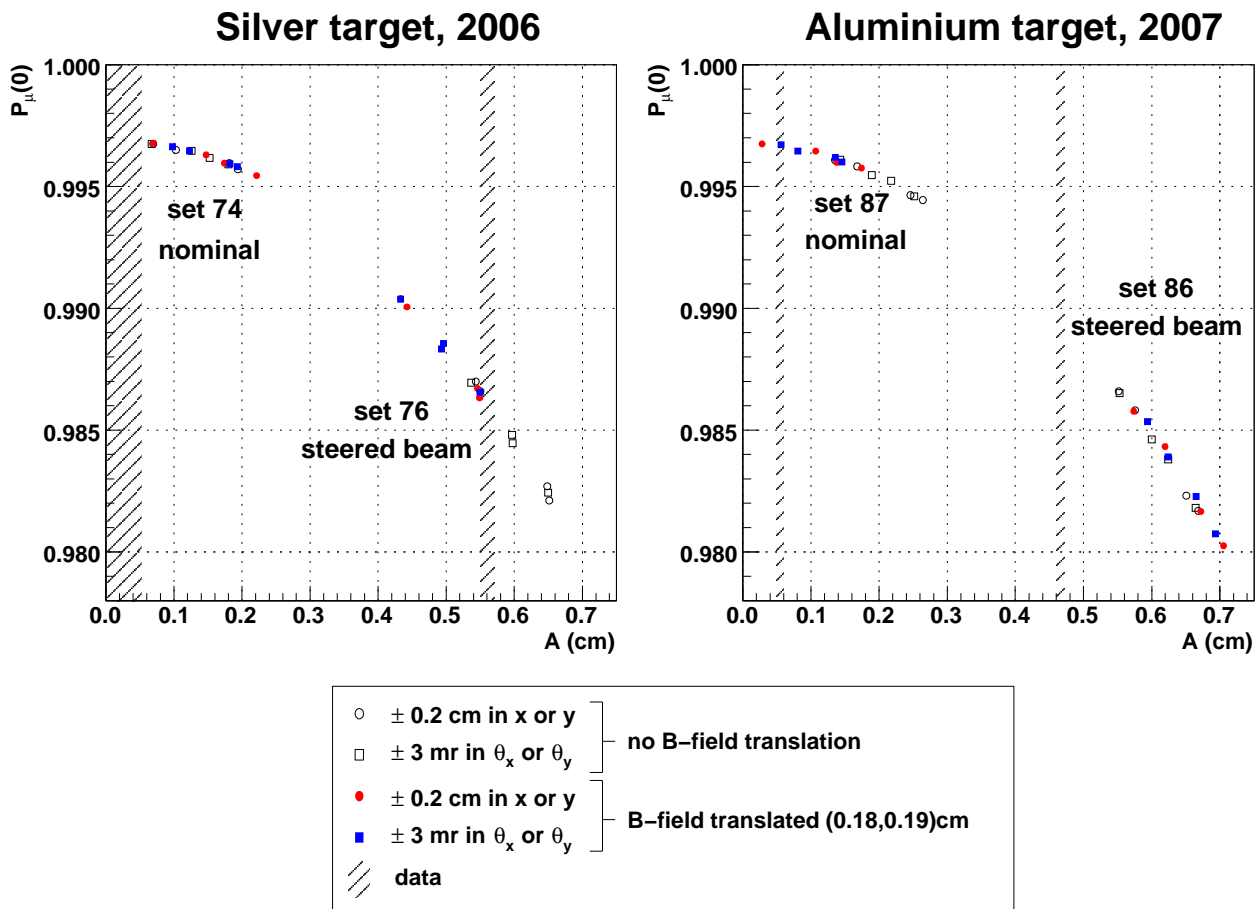


Figure 6.7: Amplitude of muon beam oscillations, A , and its relationship to $P_\mu(0)$. The combination of uncertainties in magnetic field translation and TEC position/angle allow an amplitude match to the data for two of the four sets.

set 86, there are discrepancies that confirm the earlier difficulties in matching A and ΔP_μ^{87-86} . The parameters that describe the decay of A and λ with z , A_d and λ_d in Eqs. (3.25), do not offer additional information since they are highly correlated with A and λ .

Lastly, the TEC sense planes that were used to measure the muon beam for sets 68 \rightarrow 72 were not calibrated, and instead the calibrations from another set of planes were used for the analysis. Section G.4 showed that the drift cell space-time-relationships and discriminator amplitude walk corrections were consistent between planes, but the wire time offset calibration found that the TEC modules had a rotation of between 7 and 12 mr within the TEC box. Since this angle was not determined for sets 68 \rightarrow 72, they suffer from an additional TEC angle uncertainty of ± 2.5 mr. This is smaller than the ± 3 mr used above to estimate the systematic uncertainty, so no further action has been taken.

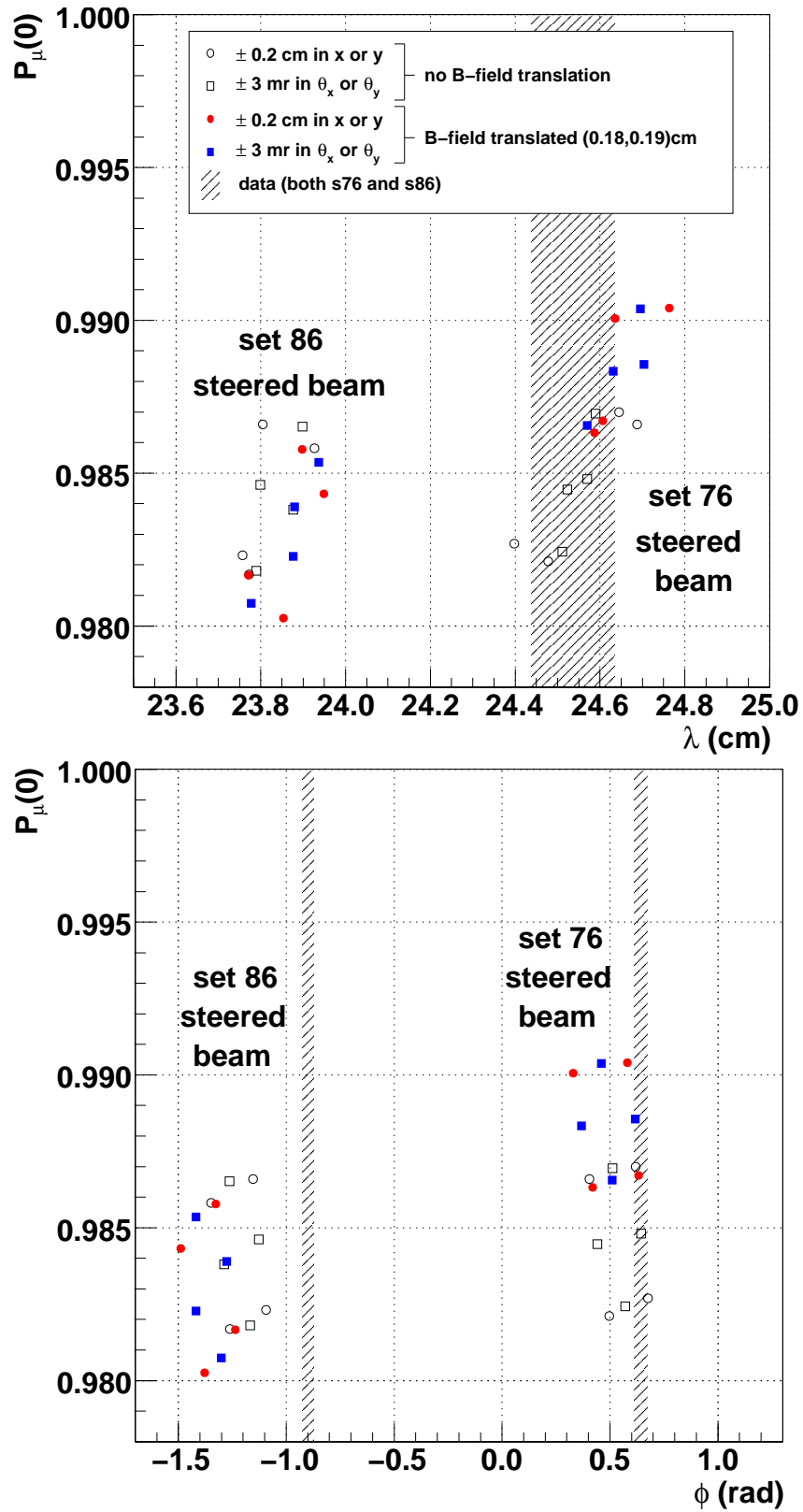


Figure 6.8: Wavelength (λ) and phase (ϕ) of the muon beam oscillations, for the steered sets.

Muon beam angular distribution width

The muons were multiple scattered as they passed through the TECs, resulting in a measured angle distribution that was too large. A GEANT3 simulation of the TECs determined that the root mean square of the angles should be reduced by a factor of $c_x = 0.6391$ in the x -module, and $c_y = 0.4795$ in the y -module to account for this multiple scattering. The dependence of $P_\mu(0)$ on the choice of c_x is shown in Fig. 6.9 for a nominal and steered beam. To an acceptable approximation, $dP_\mu(0)/dc_x$ and $d^2P_\mu(0)/dc_x^2$ are independent of the beam steering. For example, a variation of $\pm 10\%$ variation in c_x changes $P_\mu(0)$ by ${}^{+3.3}_{-3.1} \times 10^{-4}$ for the nominal case, and ${}^{+3.2}_{-2.9} \times 10^{-4}$ for the steered beam. As a result, the choice of c_x and c_y has no bearing on the comparison of ΔP_μ^{74-76} and ΔP_μ^{87-86} between data and simulation. In addition, the internal beam measurement is barely affected by c_x and c_y , and their uncertainties can be safely treated as orthogonal to the $P_\mu^\pi \xi$ systematic uncertainties that have already been evaluated⁴¹.

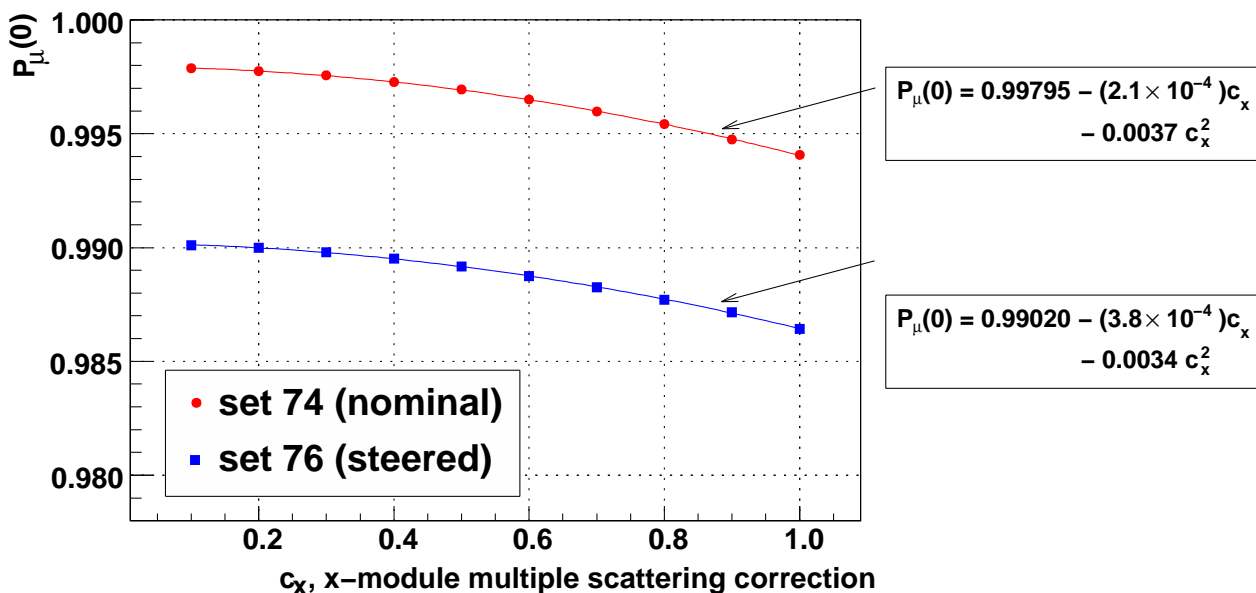


Figure 6.9: Sensitivity of $P_\mu(0)$ to c_x , the multiple scattering correction factor in the x -module. Note that the ratio $c_x/c_y = 63.91/47.95$ was maintained.

⁴¹If the ratio of c_x to c_y is maintained, and c_x is varied between 0 and 1, then the following muon beam changes are observed: the amplitude A changes by up to 0.03 cm for the steered sets, but there is no evidence of changes for the nominal sets. The wavelength and phase change by less than < 0.4 cm and 0.10 rad respectively, independent of profile. The largest position changes are 0.01 cm, again independent of profile.

The parameters c_x and c_y relied on the accuracy of multiple scattering in GEANT3. The author is unaware of any validation studies for the multiple scattering of muons with $p \approx 30$ MeV/c in thin materials (the entire TEC apparatus was equivalent to just ≈ 7 mg/cm² of material). Our most direct test of the GEANT3 accuracy used five runs with the upstream window on the TECs changed from the nominal 6 μ m of Mylar to a thicker 25 μ m (3.2 mg/cm²) window. The additional 19 μ m of material increased the scattering distribution so that

$$\theta_{\text{TECs}+25\ \mu\text{m}} \approx \sqrt{\theta_{\text{TECs}+6\ \mu\text{m}}^2 + \theta_{19\ \mu\text{m}}^2}. \quad (6.5)$$

The results for $\theta_{19\ \mu\text{m}}$ from data and simulation are shown in Table 6.6, where the simulation overestimates the root mean square width of the scattering distributions by 18.3% in the x -module and 15.6% in the y -module. This implies that the c_x and c_y factors were reliable to 17.0% (the average of the overestimate in each module), and results in a systematic uncertainty of 5×10^{-4} .

Table 6.6: Width of reconstructed angle distributions for TEC Mylar windows of thickness 6 μ m and 25 μ m. The bracketed number indicates the statistical uncertainty in the final digits.

Mylar window thickness (μ m)	RMS of θ_x (mr)		RMS of θ_y (mr)	
	data	simulation	data	simulation
6	14.50 (5)	14.10 (7)	19.79 (7)	19.89 (6)
25	17.25 (8)	17.90 (9)	22.01 (6)	22.8 (1)
\Rightarrow 19	9.3 (2)	11.0 (2)	9.6 (2)	11.1 (2)

The TEC analysis code was reviewed for this measurement, and the accuracy of the reconstruction algorithm was found to be limited by noise from the electronics. This did not affect the mean position/angle, only the width of the angular distributions. An attempt to overcome this limitation resulted in two variants of the algorithm (see Section G.3.4). Since an event-by-event investigation could not distinguish which variant was the most accurate, the difference between the two is taken as a systematic uncertainty. For all sets this difference in $P_\mu(0)$ was less than 2.2×10^{-4} , except for set 86 (steered) where $P_\mu(0)$ changed by 2.9×10^{-4} between the two variants of the algorithm. A systematic uncertainty of 2.2×10^{-4} is assigned for the nominal sets.

The width of the angular distributions depended on the mean number of hits in the final track ($\langle n_x \rangle$ in the x -module, $\langle n_y \rangle$ in the y -module), which decreased depending on the length of time that the sense planes were exposed to the beam. The same c_x and c_y correction

factors were used for all muon beam measurements, despite differences in the age of the planes, and this resulted in a systematic uncertainty. For each set, $\langle n_x \rangle$ and $\langle n_y \rangle$ are shown in Fig. 6.10. The c_x and c_y factors were tuned using set 75, which had $\langle n_x \rangle = 15.0$ and $\langle n_y \rangle = 15.9$. For all the sets, the ranges of $\langle n_x \rangle$ and $\langle n_y \rangle$ were 13.0 to 16.7, and 14.4 to 18.5 respectively, which is almost symmetric about the values used for tuning. The set 75 data were reanalysed, with hits removed at random to reduce $\langle n_x \rangle$ to 13.0 and $\langle n_y \rangle$ to 16.7. The root-mean-square reduced by 7.9% in the x -module, and 3.7% in the y -module. If the larger of these is used, then a conservative systematic uncertainty for the nominal sets due to sense plane aging is 2.6×10^{-4} .

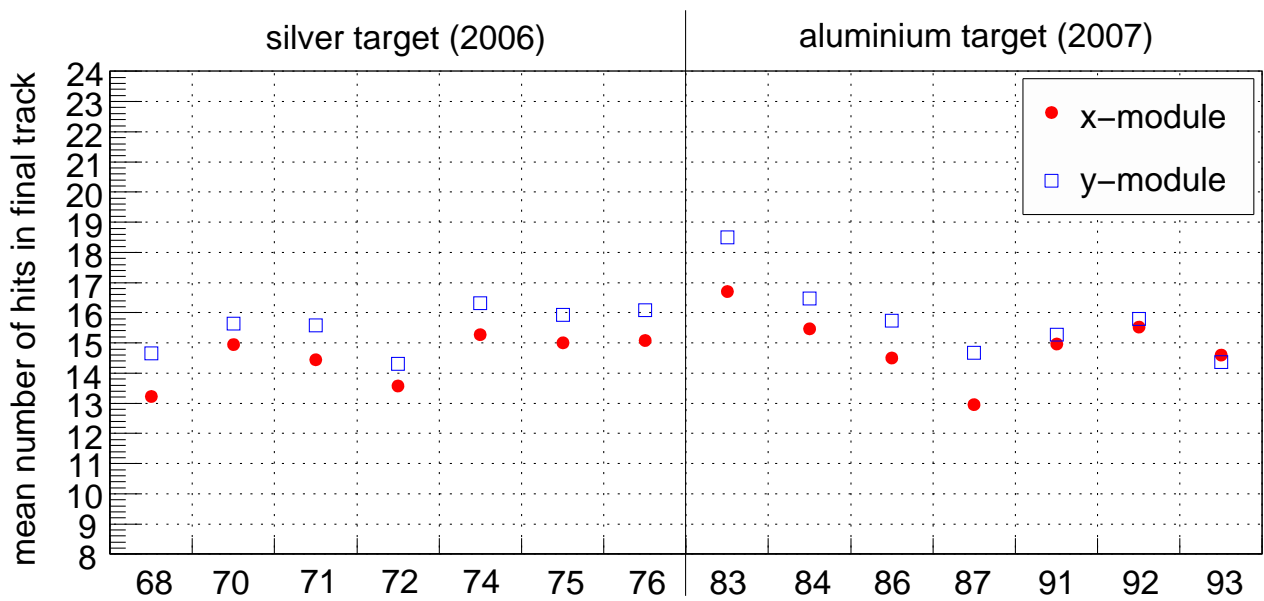


Figure 6.10: Number of hits in final TEC track, for each module. The c_x and c_y correction factors were tuned using set 75, which had $\langle n_x \rangle = 15.0$ and $\langle n_y \rangle = 15.9$.

6.3.3 Stopping material

About 80% of the muons stopped in a metal target, which also served as the shared cathode foil for the proportional chambers PC6 and PC7 (see Fig. 2.14). Events were only accepted if the muon produced a signal in PC6, but not in PC7. Muons that stopped in the PC6 gas or wires were then removed by cutting on the muon pulse width in the chamber (see Section 3.3.3). This selected a clean sample of muons that stopped in the metal foil.

The weighted asymmetry was constructed according to the method described in Section 3.6, and each data set was fit with

$$P_\mu(t) = P_\mu(0) \exp(-\lambda t). \quad (6.6)$$

The results for the time range ($1.05 < t < 9.00$) μs are shown in Table 6.7. A weighted average of these relaxation rates finds $\lambda_{\text{Ag}} = (0.840 \pm 0.072) \text{ ms}^{-1}$ and $\lambda_{\text{Al}} = (1.320 \pm 0.077) \text{ ms}^{-1}$.

Table 6.7: Relaxation rate λ for each data set. $P_\mu(t) = P_\mu(0) \exp(-\lambda t)$ has been fit over the nominal time range of ($1.05 < t < 9.00$) μs .

Set num.	Target	Description	λ (ms^{-1})	Fit quality χ^2/ndof	confidence
68	Ag	Stopping distrib. peaked $\frac{1}{3}$ into target	0.88 ± 0.21	$16.0/20 = 0.80$	0.720
70	Ag	B = 1.96 T	0.86 ± 0.17	$15.6/20 = 0.78$	0.742
71	Ag	B = 2.04 T	0.98 ± 0.18	$26.4/20 = 1.32$	0.153
72	Ag	TECs-in, nominal beam	0.93 ± 0.18	$25.9/20 = 1.29$	0.170
74	Ag	Nominal A	1.02 ± 0.22	$19.4/20 = 0.97$	0.497
75	Ag	Nominal B	0.86 ± 0.18	$12.9/20 = 0.65$	0.880
76	Ag	Steered beam A	0.32 ± 0.20	$12.5/20 = 0.63$	0.897
83	Al	Downstream beam package in place	1.41 ± 0.18	$32.7/20 = 1.63$	0.037
84	Al	Nominal C	1.26 ± 0.19	$24.4/20 = 1.22$	0.225
86	Al	Steered beam B	1.29 ± 0.16	$26.5/20 = 1.33$	0.149
87	Al	Nominal D	1.28 ± 0.18	$13.9/20 = 0.70$	0.833
91	Al	Lower momentum I	1.65 ± 0.33	$20.1/20 = 1.01$	0.449
92	Al	Lower momentum II	1.30 ± 0.29	$16.1/20 = 0.81$	0.708
93	Al	Lower momentum III	1.25 ± 0.22	$15.1/20 = 0.76$	0.770

The simulation used preliminary values of $\lambda_{\text{Ag}} = 0.732 \text{ ms}^{-1}$ and $\lambda_{\text{Al}} = 1.169 \text{ ms}^{-1}$. The weighted asymmetry analysis was applied to the simulation, and found $\lambda_{\text{Ag}} = (0.625 \pm 0.065) \text{ ms}^{-1}$ and $\lambda_{\text{Al}} = (1.104 \pm 0.076) \text{ ms}^{-1}$, using the nominal time range of ($1.05 < t <$

9.00) μs . These results are 1.6σ and 0.9σ below the true values in the simulation, which indicates a potential small and subtle bias in analysis. An independent investigation found that an unbiased muon lifetime measurement required a time fiducial of $(2.00 < t < 9.00) \mu\text{s}$. If the asymmetry analysis is applied to the simulation with a lower time cut of $2.00 \mu\text{s}$, then $\lambda_{\text{Ag}} = (0.614 \pm 0.087) \text{ms}^{-1}$ and $\lambda_{\text{Al}} = (1.19 \pm 0.10) \text{ms}^{-1}$, which are closer to the true values.

The data were reanalysed with the time range of $(2.00 < t < 9.00) \mu\text{s}$, yielding the experiment's most precise unbiased results for the relaxation rates,

$$\lambda_{\text{Ag}} = (0.94 \pm 0.10) \text{ms}^{-1}, \quad (6.7)$$

$$\lambda_{\text{Al}} = (1.20 \pm 0.10) \text{ms}^{-1}. \quad (6.8)$$

Note that these are consistent with the $\mu^+\text{SR}$ results from Section H.8:

$$\lambda_{\text{Ag}} = (0.9 \pm 0.2 \text{ (stat.)} \pm 0.2 \text{ (syst.)}) \text{ms}^{-1}, \quad (6.9)$$

$$\lambda_{\text{Al}} = (1.3 \pm 0.2 \text{ (stat.)} \pm 0.3 \text{ (syst.)}) \text{ms}^{-1}. \quad (6.10)$$

The simulation used an inaccurate λ value, and as a result $P_\mu^\pi \xi$ must be corrected. The effect on the spectrum of a change in λ can be calculated using

$$\frac{\int_{t_1}^{t_2} N(t) \cdot P_\mu(0) \exp(-\lambda_2 t) dt}{\int_{t_1}^{t_2} N(t) dt} - \frac{\int_{t_1}^{t_2} N(t) \cdot P_\mu(0) \exp(-\lambda_1 t) dt}{\int_{t_1}^{t_2} N(t) dt}, \quad (6.11)$$

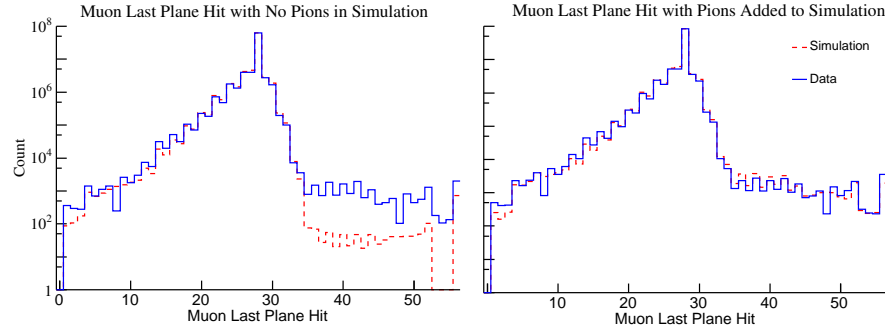
where $N(t) = N(0) \exp(-t/\tau_\mu)$ and τ_μ is the muon lifetime, and λ_1 and λ_2 are the relaxation rates between which the correction is being made. The common $P_\mu(0)$ factor is close to 1.0, and its choice has a negligible impact on the correction. The simulation's P_μ must be corrected by -6.3×10^{-4} for Ag ($\lambda_1 = 0.732 \text{ms}^{-1}$, $\lambda_2 = 0.94 \text{ms}^{-1}$) and -0.9×10^{-4} for Al ($\lambda_1 = 1.169 \text{ms}^{-1}$, $\lambda_2 = 1.20 \text{ms}^{-1}$). The statistical uncertainty in determining λ from the data causes a P_μ uncertainty of 3.0×10^{-4} for both targets, again using Eq. (6.11).

The simulation found that about 0.2% of muons entered PC7, but did not have enough energy to produce a signal. The depolarisation within the PC gas ($\text{CF}_4/\text{isobutane}$) and wires was about 3%. The systematic uncertainty due to these stops is therefore $\approx 0.2\% \times 3\% = 0.6 \times 10^{-4}$, which is negligible.

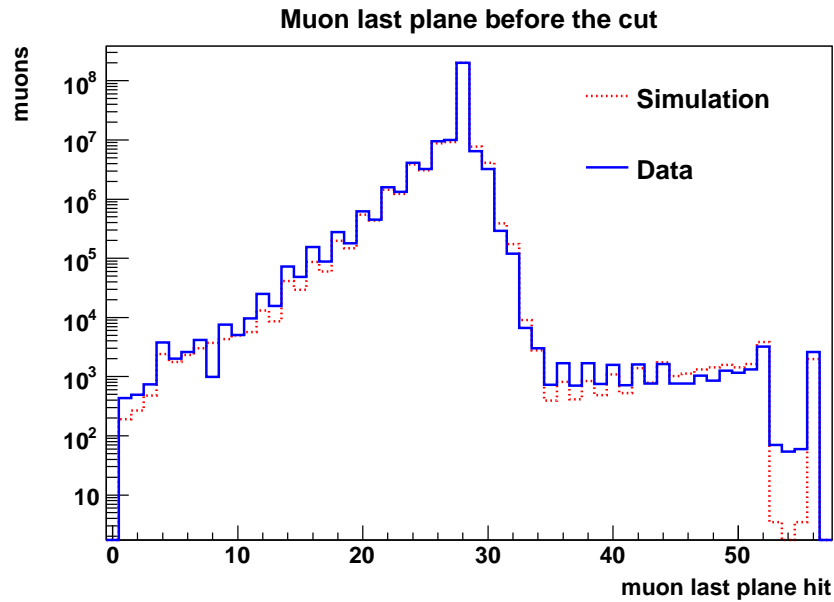
6.3.4 Background muon contamination

In the previous $P_{\mu}^{\pi} \xi$ analysis, the number of muons downstream of the stopping target did not agree in the data and simulation; this is demonstrated in Fig. 6.11(a). The stopping distributions were consistent if pion decays were simulated in the upstream “beam package” area. Improvements in the current analysis have removed most of the discrepancy, without having to include the additional pion decays; the modern agreement is demonstrated in Fig. 6.11(b).

The residual discrepancy in Fig. 6.11(b) introduced an uncertainty in the muon stopping distribution, which must be matched to prevent a bias in the muon polarisation, since high angle muons that undergo more depolarisation are preferentially stopped further upstream. Specifically, the simulation needed an extra 1.9 mg/cm^2 of material to match the stopping distribution in the data (see Section 2.11), and we could not be sure whether this was justified. Fortunately the effect on the polarisation was minimal: including an extra 1.9 mg/cm^2 in the simulation introduced a systematic uncertainty of just 1×10^{-4} for all the beam profiles except set 72 (TECs-in), which had an uncertainty of 4×10^{-4} .



(a) Comparison of muon stopping distribution from the previous analysis (originally Fig. 6.9 from Ref. [57]). The mismatch between data and simulation is resolved by adding muons from pion decays in the M13 beam line.



(b) The same figure re-made for the current analysis. In this figure there are no additional pion decays added.

Figure 6.11: Background muon contamination in the two $P_\mu^\pi \xi$ analyses.